analytical chemistry

pubs.acs.org/ac

Article

Biosensor-Enabled Deconvolution of the Avidity-Induced Affinity Enhancement for the SARS-CoV-2 Spike Protein and ACE2 Interaction

Aspen Rene Gutgsell, Anders Gunnarsson, Patrik Forssén, Euan Gordon, Torgny Fornstedt, and Stefan Geschwindner*

Cite This: *Anal. Chem.* 2022, 94, 1187−1194

Read Online

ACCESS | Metrics & More | Article Recommendations | Supporting Information

ABSTRACT: Avidity is an effective and frequent phenomenon employed by nature to achieve extremely high-affinity interactions. As more drug discovery efforts aim to disrupt protein−protein interactions, it is becoming increasingly common to encounter systems that utilize avidity effects and to study these systems using surface-based technologies, such as surface plasmon resonance (SPR) or biolayer interferometry. However, heterogeneity introduced from multivalent binding interactions complicates the analysis of the resulting sensorgram. A frequently applied practice is to fit the data based on a 1:1 binding model, and if the fit does not describe the data adequately, then the experimental setup is changed to favor a 1:1 binding interaction. This reductionistic approach is informative but not always biologically relevant. Therefore, we aimed to develop an SPR-based assay that would reduce the heterogeneity to enable the determination of the kinetic rate constants for multivalent binding interactions using the severe acute respiratory syndrome coronavirus 2 (SARS-CoV-2) spike protein and the human receptor angiotensin-converting enzyme 2 (ACE2) as a model system. We employed a combinatorial approach to generate a sensor surface that could distinguish between monovalent and multivalent interactions. Using advanced data analysis algorithms to analyze the resulting sensorgrams, we found that controlling the surface heterogeneity enabled the deconvolution of the avidity-induced affinity enhancement for the SARS-CoV-2 spike protein and ACE2 interaction.

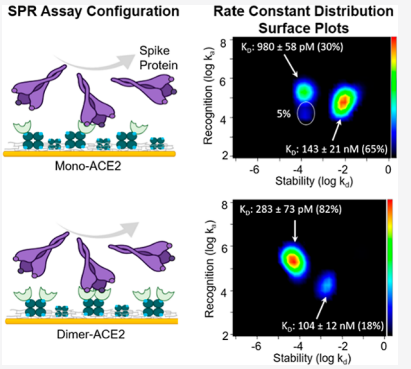

Proteins can undergo vast conformational rearrangements to form complex biomolecular interactions. Protein−protein interactions can range from transient, low-affinity interactions to long-lived complexes displaying sub-picomolar affinity.[1] One of the many strategies that nature employs to achieve such high-affinity interactions is through avidity.[2] Avidity is a phenomenological macroscopic parameter linked to several microscopic binding events that occur between proteins via multiple interaction sites.[2] Upon the engagement of one binding site, the local concentration of the ligand increases, and thus, the probability of binding or rebinding is significantly enhanced.[2] This results in complexes with long residence times whose binding curves do not follow a single exponential time course.[3] Therefore, quantifying the kinetic rate constants for these multivalent biomolecular interactions is very challenging and often results in erroneous affinity estimates when applying a simple 1:1 binding model.[3,4] A prominent example of this can be found in the recent literature studies describing the binding affinity of the severe acute respiratory syndrome coronavirus 2 (SARS-CoV-2) spike protein for the human receptor angiotensin-converting enzyme 2 (ACE2).[5−14]

The COVID-19 pandemic caused by SARS-CoV-2 has sparked a global initiative to understand the mechanism of action of this highly infectious disease.[15] Similar to other coronaviruses, the surface of SARS-CoV-2 is decorated with glycosylated spike (S) proteins that bind host ACE2 receptors to mediate the fusion of viral and host cell membranes.[9,12] The S protein is an obligate trimer that engages ACE2 via three N-terminal receptor-binding domains (RBDs). The ability of each RBD to engage the ACE2 receptor directly corresponds to its conformational state. The RBD is thought to bind ACE2 when it is in the "up" conformation or the active state.[16,17] Although many high-resolution structural images depict the S protein with one RBD bound to one ACE2 ectodomain, there is additional structural evidence that three RBDs can engage up to three ACE2 molecules simultaneously.[16,18−20]

Although the SARS-CoV-2 S protein shares 76% sequence identity with another closely related coronavirus, SARS-CoV, SARS-CoV-2 has proven to be far more infective/trans-

Received: October 8, 2021
Accepted: December 15, 2021
Published: December 29, 2021

missible.[6,13,15] This has spurred several researchers to hypothesize that the SARS-CoV-2 S protein has a higher affinity for ACE2 than the SARS-CoV S protein. Several studies have utilized sensor-based technologies to answer this question, but thus far, the data have been inconclusive.[6,7,10,12] This likely stems from the fact that the majority of these assays are simplified to only measure the 1:1 binding interaction between an isolated RBD and a single ACE2 monomer.[7,9,12] In reality, the functional affinity is likely to be significantly higher due to avidity effects. Therefore, our goal was to develop a biosensor-based method that could better distinguish between monovalent and avidity-enhanced interactions using the SARS-CoV-2 S protein and ACE2 interaction as a model system. We employed a multistep approach to create a sensor that would favor a monovalent interaction event between the S protein and ACE2, as well as a surface that favors the generation of multivalent interactions. To allow for the accurate estimation of the functional affinity for the multivalent interaction, the data were fitted using advanced models that account for heterogeneous binding and provide a two-dimensional distribution analysis of the association and dissociation rate constants.[21,22] Using this rate constant distribution (RCD) approach, we found that reducing the surface heterogeneity greatly facilitated the deconvolution of the monovalent and multivalent binding events.

EXPERIMENTAL SECTION

Materials. Unless otherwise stated, all chemicals were purchased from Sigma-Aldrich. Switchavidin was purchased from BioMediTech (Tampere, Finland) and produced as previously described by Taskinen and colleagues.[23]

Expression and Purification of SARS-CoV-2 and ACE2 Ectodomains. Full-length SARS-CoV-2 S protein and the isolated RBD domain containing a C-terminal 8x-polyhistidine tag were transiently expressed in Chinese hamster ovarian EBNA GS (CHO) and Expi293F ULK1 knockout (Vulko293) cells, respectively. CHO cells were maintained in a CD CHO medium (10743-029, Gibco, ThermoFisher) supplemented with 100 μg/mL hygromycin and 25 μM L-methionine sulfoximine (M5379, Sigma). Vulko293 cells were maintained in an Expi293 expression medium (A14351, Gibco, ThermoFisher). Both cell lines were transfected with their respective plasmids using the PEI MAX transfection reagent (24765, Polysciences). S protein or RBD domain-containing media were collected and incubated with Ni Sepharose Excel (Cytiva) overnight at 4 °C. The resin was washed with buffer A (20 mM Tris, pH 7.5, 500 mM NaCl, and 20 mM imidazole) and eluted with buffer B (20 mM Tris, pH 7.5, 500 mM NaCl, and 400 mM imidazole). The eluate was directly loaded onto an equilibrated Superdex 26/600 200 (Cytiva) column and eluted in 1.6 mL fractions in buffer C (20 mM HEPES pH 7.4, 250 mM NaCl, and 5% glycerol). Fractions containing the S protein or RBD domain were pooled and concentrated to a final concentration of 1 mg/mL.

The human ACE2 ectodomain containing a C-terminal 8x-polyhistidine tag and an avi-tag was transiently expressed in Vulko293 cells. ACE2-containing media were incubated with Ni Sepharose Excel (Cytiva), washed with buffer A (20 mM HEPES pH 7.4, 250 mM NaCl, 5% glycerol, and 10 mM imidazole), and eluted with buffer B (20 mM HEPES, pH 7.4, 250 mM NaCl, 5% glycerol, and 400 mM imidazole). The eluate was directly loaded onto a Superdex 26/600 200 (Cytiva) column and eluted in buffer C. Fractions containing ACE2 were pooled and concentrated to a final concentration of 4 mg/mL. ACE2 was biotinylated *in vitro* using recombinant BirA.

Mass Photometry of SARS-CoV-2 and ACE2. All samples were measured in 1× HBS-N buffer (10 mM HEPES, pH 7.4, and 150 mM NaCl) using the Refeyn OneMP mass photometer (Refeyn Ltd.) with a 60 s acquisition time. The resulting histograms were fitted to Gaussian distributions using DiscoverMP (Refeyn Ltd.) to extract the peak contrast and relative amount of each peak (n = 3). The contrast-to-mass conversion was achieved by calibration using a NativeMark protein ladder (ThermoFisher Scientific). Three protein species (with specified masses) were fitted to corresponding Gaussian distributions to extract a linear relation between the mass and contrast (Figure S1). The S protein trimer was diluted to a concentration corresponding to 30 nM, and the ACE2 complex was investigated by adding a 2- or 3-fold excess of ACE2 to the S protein.

Generation of ACE2−Switchavidin Complexes. ACE2 and switchavidin were mixed in stoichiometric ratios of 1:1 and 1:2 in 10 mM HEPES, pH 7.4, and 150 mM NaCl. The mixtures were incubated at room temperature for 30 min. The complex formation was monitored using a Refeyn OneMP mass photometer (Refeyn Ltd.). Then, the samples were diluted to 12 nM and measured as described above.

Individual ACE2−switchavidin complexes were isolated using high-resolution size -exclusion chromatography and mass photometry. Briefly, the mixture was injected and run over a Superdex 30 Increase 3.2/300 column (Cytiva) at 50 μL/min and collected in 30 μL fractions. The protein concentration in individual fractions was checked in individual fractions using the NanoDrop One spectrophotometer (ThermoFisher Scientific), and ACE2−switchavidin stoichiometries were measured using mass photometry as described above. Fractions with more than 90% of the species corresponding to one ACE2 molecule bound to one switchavidin molecule (a total mass of 148 kDa) were used as the monomeric ACE2 species in subsequent surface plasmon resonance (SPR) assays. Fractions with more than 90% of the species corresponding to multiple ACE2 molecules bound to one switchavidin molecule (total masses of 232, 320, and 411 kDa) were used as the multivalent ACE2 species in subsequent SPR assays. Remaining samples were flash frozen and stored at −80 °C.

SPR Assays. All SPR experiments were conducted on a BIAcore S200 instrument (Cytiva) using 10 mM HEPES, pH 7.4, 150 mM NaCl, and 0.05% Tween-20 (HBS-P+) as the running buffer.

Single-cycle kinetic experiments were conducted using a sensor with $Ni2^+$ ions complexed on a two-dimensional chelating surface (NIP, Xantec Bioanalytics GmbH) at 25 °C. Prior to the ligand immobilization, the sensor was washed with 300 mM EDTA, pH 8.3, and loaded with $Ni2^+$ ions by injecting a 500 nM solution of $NiCl_2$ in the running buffer for 1 min. The surface was activated for 5 min with 0.05 M N-hydroxysuccinimide and 0.2 M 1-ethyl-3-(3-dimethylaminopropyl)carbodiimide, followed by an injection of the respective protein (his-tagged ACE2, his-tagged SARS-CoV-2 RBD, or his-tagged SARS-CoV-2 S protein) at a concentration of 20−50 ng/mL and using a contact time of 1−2 min to achieve the desired densities of 150−300 RU. This was followed by the deactivation of residual esters with 0.5 M ethanolamine hydrochloride, pH 8.5, for 5 min. Reference

https://doi.org/10.1021/acs.analchem.1c04372
Anal. Chem. 2022, 94, 1187−1194

surfaces were prepared accordingly, omitting the injection of protein over the activated reference surface. For the surfaces with the SARS-CoV-2 S protein and SARS-CoV-2 RBD as the surface-immobilized ligand, increasing concentrations (8, 20, 80, 200, 800, and 2000 nM) of untagged ACE2 were iteratively injected with a 120 s contact time during each injection, followed by a 1200 s dissociation phase. For the surface with the immobilized ACE2 protein as the ligand, increasing concentrations (10, 30, 100, 200, 400, and 1000 nM) of the untagged SARS-CoV-2 S protein were iteratively injected with a 60 s contact time during each injection, followed by a 1200 s dissociation phase. All resulting sensorgrams were reference- and blank-subtracted prior to fitting.

Multicycle kinetic experiments were conducted using a biotin-coated sensor chip (BHC30M Xantec Bioanalytics GmbH) at 25 °C. Prior to the ligand immobilization, the chip was washed with 50 mM NaOH, 1 M NaCl, and 2.5% citric acid, 0.25% sodium dodecyl sulfate (SDS). 1000 RU of switchavidin was immobilized across all channels followed by the immobilization of 30 RU of monomeric ACE2−switchavidin on flow channel 2 (Fc2) and 70 RU of dimeric ACE2−switchavidin on Fc4. The SARS-CoV-2 S protein was injected in 5-fold dilutions for 600 s and allowed to dissociate for 2000 s before surface regeneration with 2.5% citric acid, 0.25% SDS. The resulting sensorgrams were reference- and blank-subtracted prior to fitting.

Fitting of SPR Sensorgrams. All SPR data were fitted using a 1:1 binding model (BIAcore Evaluation Software, Cytiva). If the data could not be described with a 1:1 binding model, then the data were fitted using RCDs or the strategy described in references 4 and 5. An RCD is a bivariate distribution of association rates k_a and dissociation rates k_d that describes the measured binding curve, and it can be visualized as an intensity image. An RCD is the solution to a Fredholm integral equation of the first kind. We used InteractionMap (Ridgeview Diagnostics, AB) or the adaptive interaction distribution algorithm (AIDA) to calculate the RCDs, and they differ slightly in their approach. Each method has been described and validated previously.[5,21,22]

RESULTS AND DISCUSSION

SARS-CoV-2 Spike Ectodomain Samples Heterogeneous ACE2-Binding Conformations in Solution. Numerous cryogenic electron microscopy studies have reported structures of the trimeric S protein bound to the ACE2 ectodomain. The majority of these structures depict one trimeric S protein bound to one ACE2 molecule, but additional structures have shown that up to three ACE2 molecules can bind to one S protein at a time.[6,16,24] To determine whether these stoichiometries are also observed in solution, we utilized mass photometry to directly measure the S protein−ACE2 complex. Mass photometry is a technology that utilizes the principles of interference reflection microscopy and interferometric scattering microscopy to enable the mass measurement of single, native protein molecules in solution.[25]

In agreement with the size-exclusion chromatography data, we confirmed that the full-length S protein is trimeric in solution with a mass corresponding to that of three glycosylated monomers, approximately 165 kDa each (Figure 1A). The purified ACE2 ectodomain was also confirmed to be monomeric with a glycosylated molecular weight of approximately 87 kDa (Figure 1B). Upon mixing the S protein with an excess of ACE2, we found evidence that the S protein

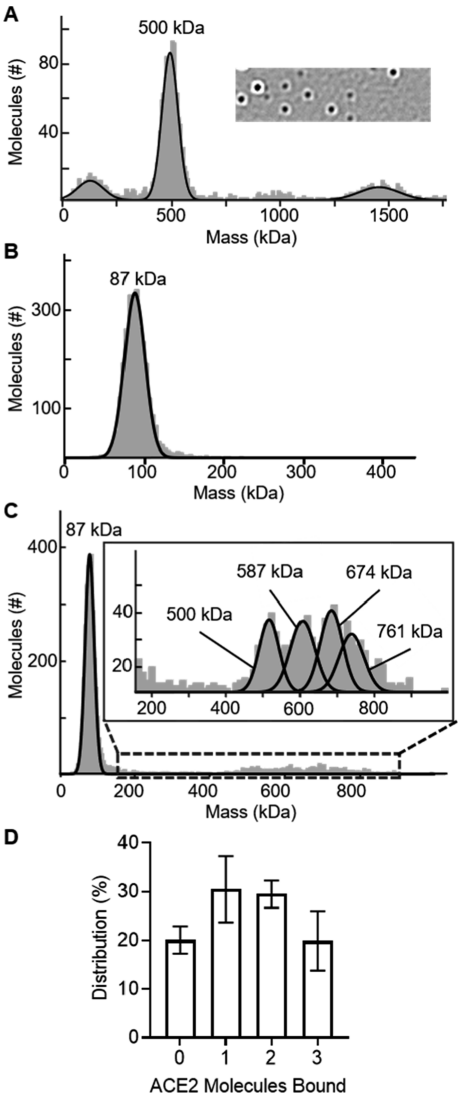

Figure 1. Mass photometry reveals that the SARS-CoV-2 spike ectodomain is multivalent for ACE2 binding. (A) Glycosylated SARS-CoV-2 S protein is a trimer corresponding to a molecular weight of approximately 500 kDa with a monomeric weight of 140 kDa. Inset depicts a representative differential interferometric scattering image with single molecules detected. (B) Glycosylated ACE2 ectodomain is monomeric with a molecular weight of 87 kDa. (C) Inset depicts the S protein−ACE2 complex formation with masses corresponding to zero, one, two, and three ACE2 molecules bound to the S protein in real time. (D) Relative distribution of ACE2-bound S protein species from the inset shown in C with error bars representing the standard deviation of $n = 3$.

samples at least four different conformational states, of which three are defined via different ACE2-bound states (Figure 1C). Masses corresponding to zero, one, two, and three ACE2 molecules bound to a single S protein were detected (Figure 1C). In these experiments, we observe nearly an equal distribution of each "ACE2-binding" competency, which relates to S protein RBDs sampling different up and down conformations (Figure 1D). These data are in agreement with a recent publication by Lu and colleagues, which demonstrated that the SARS-CoV-2 S protein is present in at least four distinct conformational states in solution, which correspond to its ACE2-binding competency.[20]

https://doi.org/10.1021/acs.analchem.1c04372
Anal. Chem. 2022, 94, 1187−1194

Evidence of Monovalent and Multivalent Interactions between the S Protein and ACE2. We employed several SPR assay formats to first replicate the kinetic data observed in other studies. In one format, the binding of the isolated S protein RBD to monomeric ACE2 was measured. In agreement with previous studies, the curve for ACE2 binding to the monomeric S protein RBD-coated surface follows a single exponential time course and is well-described by a 1:1 binding model (Figure S2A,B).[7,9,13] As expected, this binding curvature is consistent when the assay is inverted such that the RBD is injected over an ACE2-coated surface (Figure S2C,D). The measured affinity for the S protein RBD−ACE2 interaction is approximately 16.6 nM.

In the other format, we measured the binding of the full-length trimeric S protein to monomeric ACE2. Increasing concentrations of monomeric ACE2 were injected over a trimeric S protein-coated surface (Figure 2A). Similar to sensorgrams generated from the RBD-coated surface, the binding curve fit a 1:1 binding model with an estimated K_d of 60 nM (Figure 2A). This is suggestive of monovalent binding between one ACE2 monomer and one RBD within the S protein trimer.

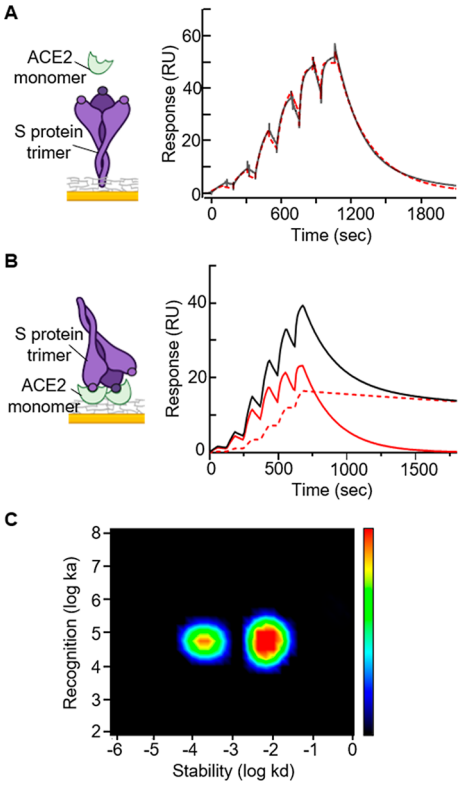

Figure 2. Multivalent interactions observed upon ACE2 immobilization. (A) 300 RU of the trimeric SARS-CoV-2 S protein (purple) was tethered to a NIP sensor (gold) and increasing concentrations of monomeric ACE2 (light green) was injected over the surface as the analyte. The resulting sensorgram (gray) is well-described by a 1:1 binding model (dashed red line) and has an estimated K_d of 60 nM. (B) Inverted assay where 150 RU of ACE2 (light green) was tethered to a NIP sensor (gold) and increasing concentrations of trimeric S protein (purple) was injected over the surface as the analyte. The resulting sensorgram (gray) is best described with a heterogeneous binding model that fits for a monovalent component (solid red line) and a multivalent binding component (dashed red line). (C) InteractionMap for the sensorgram depicted in (B) resolved two interactions with red corresponding to strong contributing interactions and blue corresponding to weak contributing interactions. Schematics were created with BioRender.com.

Upon inverting the assay such that ACE2 was tethered to the surface, the binding curve deviated from a single exponential time course and could no longer be described by a 1:1 binding model (Figure 2B). Therefore, we used the InteractionMap (IM) platform to fit the data. The IM is an RCD-based approach that considers complex binding data to be the summation of kinetically distinct 1:1 binding interactions that occur in parallel.[22] Therefore, the measured curve is approximated using the sum of a range of theoretical binding curves and fitted using a nonlinear algorithm. Using this analysis, two interactions were resolved with approximately 62% of the signal in the measured sensorgram accounting for a 129 nM affinity interaction, whereas the remaining 38% was attributed to a 4 nM affinity interaction (Figure 2C). It is important to note that although the resolved interactions differ in their dissociation rate constants, the differences in the association rate constants are impossible to estimate since the single-cycle kinetic data do not reach the steady-state equilibrium. Therefore, to better resolve the data, one would need to perform multicycle kinetic experiments with a sufficiently long injection time to reach the steady-state equilibrium.

Generation of a Custom Sensor Surface to Facilitate SPR Data Deconvolution. To better resolve the kinetic rate constants for the monovalent and multivalent interactions, we performed multicycle kinetic assays with sufficiently long injection times to reach the steady-state equilibrium. Surface regeneration was required after each injection given the near irreversible binding component observed from the trimeric S protein binding to the tethered ACE2. Switchavidin has been shown to be a valuable tool for reversible immobilization in that it not only retains a high-affinity biotin−avidin interaction resulting in a very stable baseline but also rapidly dissociates from biotin when exposed to acidic conditions.[26] By using switchavidin to tether the biotinylated ACE2 to a biotin-coated surface, the surface could be completely regenerated after each S protein injection in order to provide a fresh and unaltered surface for subsequent analyte injections. This novel approach enables more reliable quantification of the interaction strength as particular long-lived complexes with very tight interactions would otherwise reduce the number of accessible surface binding sites in an uncontrolled fashion during iterative analyte injections.

Switchavidin also enabled us to generate an ACE2-coated surface that could better distinguish between the monovalent S protein interaction and the multivalent interaction. For the monovalent interaction, the aim was to generate a homogenous biosensor surface with monomeric ACE2 molecules with such a large intermolecular distance that it should be sterically impossible for the S protein to bind more than a single ACE2 molecule at a time. Likewise, for the multivalent interaction, the aim would be to provide a surface coated with dimeric ACE2 molecules that are close enough in proximity such that two RBDs from the same trimeric molecule can bind. Therefore, we utilized switchavidin to scaffold ACE2 in a desirable configuration and isolated ACE2 pseudo-oligomers using size-exclusion chromatography for sample separation/preparation and mass photometry for sample analysis.[23,26] First, the biotinylated ACE2 was premixed with an excess of switchavidin to allow for complex formation and verified using

https://doi.org/10.1021/acs.analchem.1c04372
Anal. Chem. 2022, 94, 1187−1194

mass photometry (data not shown). Then, high-resolution size-exclusion chromatography was used to separate the species where one ACE2 molecule was bound to one switchavidin, herein referred to as monomeric ACE2, from the species where two ACE2 molecules were bound to one switchavidin molecule, herein referred to as dimeric ACE2 (Figure 3A).

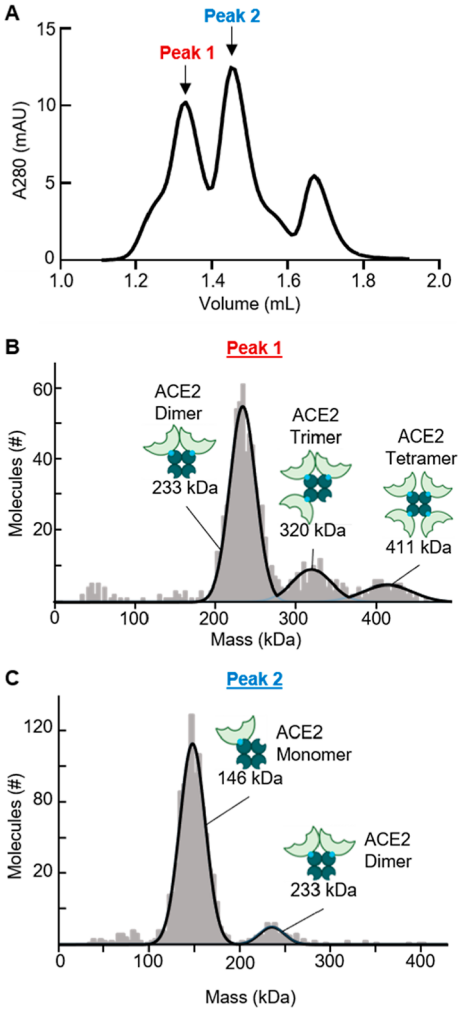

Figure 3. Isolation of ACE2−switchavidin complexes. (A) High-resolution size-exclusion chromatography was used to separate a mixture of switchavidin alone (71 kDa, teal), one ACE2 molecule bound to one switchavidin (146 kDa, green), two ACE molecules bound to one switchavidin (233 kDa), and so on. (B,C) Mass photometry data from individual S fraction(s) from peak 1 (B) and peak 2 (C) that were selected for subsequent SPR experiments.

Then, we used mass photometry to directly identify the ACE2−switchavidin composition of each fraction from size exclusion (Figure 3B,C). Fractions in which at least 90% of the sample population had a mass corresponding to that of monomeric ACE2 (Figure 3B) and or dimeric/trimeric ACE2 (Figure 3C) were subsequently immobilized on a biotin-coated sensor for multicycle kinetic studies using SPR.

SPR Using Scaffolded ACE2 to Differentiate between Monovalent and Multivalent S Protein Binding. Multicycle kinetic experiments began by immobilizing 1000 RU of switchavidin to block potential "hot spots" on the sensor surface where several ACE2-switchavidin complexes could bind in close proximity. Then, approximately 30 RU of monomeric ACE2 was immobilized on one channel and 70 RU of dimeric ACE2 was immobilized on another channel (Figure 4A,B). The difference in ACE2 response units corresponds to the mass difference between monomeric and dimeric ACE2 such that approximately the same molarity of protein complexes was immobilized on each surface. Then, serial dilutions of the full-length SARS-CoV-2 S protein were injected for 600 s, followed by a 2100 s dissociation step (Figure 4C,D). The rate of S protein dissociation from the dimeric ACE2 surface is significantly reduced in comparison to that from the monomeric ACE2 surface (Figure 4C,D). Interestingly, some multivalent interactions are present on the monomeric ACE2 surface, as evident from the biphasic dissociation phase (Figure 4C). Given the general inability to spatially control where monomeric ACE2 molecules were tethered on the surface and the presence of a small amount of dimeric ACE2 species that were detected via mass photometry (Figure 3B), it is understandable that conditions for some multivalent S protein interactions are still present on the monomeric ACE2 surface. Despite observing a signal from multivalent interactions on the monomeric ACE2 surface, one can appreciate that the residence time of the S protein on the dimeric ACE2 surface is similar to that of irreversible binding, suggesting that there is an extremely high-affinity interaction between the trimeric S protein and oligomeric ACE2.

To best describe the data from the monomeric ACE2 and dimeric ACE2 surface, we employed RCD analysis. Similar to the single-cycle kinetic analysis, the IM platform identified two contributing interactions with dissociation rate constants similar to those observed in the single-cycle kinetic analysis (Figures 2C and 4E,F). However, by allowing the association to reach the steady-state equilibrium, we were able to resolve different association rate constants for each interaction on the monomeric and dimeric surface (Figure 4E,F). On the monomeric ACE2 surface, approximately 65% of the binding signal originated from an interaction with an affinity constant of 143 nM and 30% of the signal originated from a 980 pM affinity interaction (Figure 4E). Interestingly, there was a third interaction displaying a quite similar dissociation rate but a much slower association rate in comparison to the higher-affinity interaction that accounts for approximately 5% of the binding signal (Figure 4E). This could represent an intermediate step where the S protein undergoes a conformational change that arranges more than one RBD in an upward, ACE2-binding competent position. In contrast, the intermediate interaction is not detected on the dimeric ACE2 surface, rather 82% of the signal from the sensorgram accounts for a 283 pM affinity interaction and 18% of the signal accounts for a 104 nM interaction (Figure 4F). It is possible that the third interaction is still present on the surface containing the ACE2 dimer, but the signal is occluded by the high-affinity pM interaction (Figure 4F).

Another RCD approach, developed by Forssén et al., uses a different algorithm to enhance the resolution of the data and has previously been employed to analyze the published ACE2 and SARS-CoV-2 RBD sensorgrams.[5,21] This method utilizes the AIDA. For this analysis, the heterogeneity is estimated by plotting $\ln(R/R_0)$ versus time using the data from the 600 nM S protein condition (Figure S3A,B). Then, as in the IM, the RCD is calculated but by using the AIDA instead (Figure S3C,D). Next, the rate constants are estimated by fitting a suitable interaction model for each sensorgram. Lastly, the individual rate constants are clustered to obtain the estimates

https://doi.org/10.1021/acs.analchem.1c04372
Anal. Chem. 2022, 94, 1187−1194

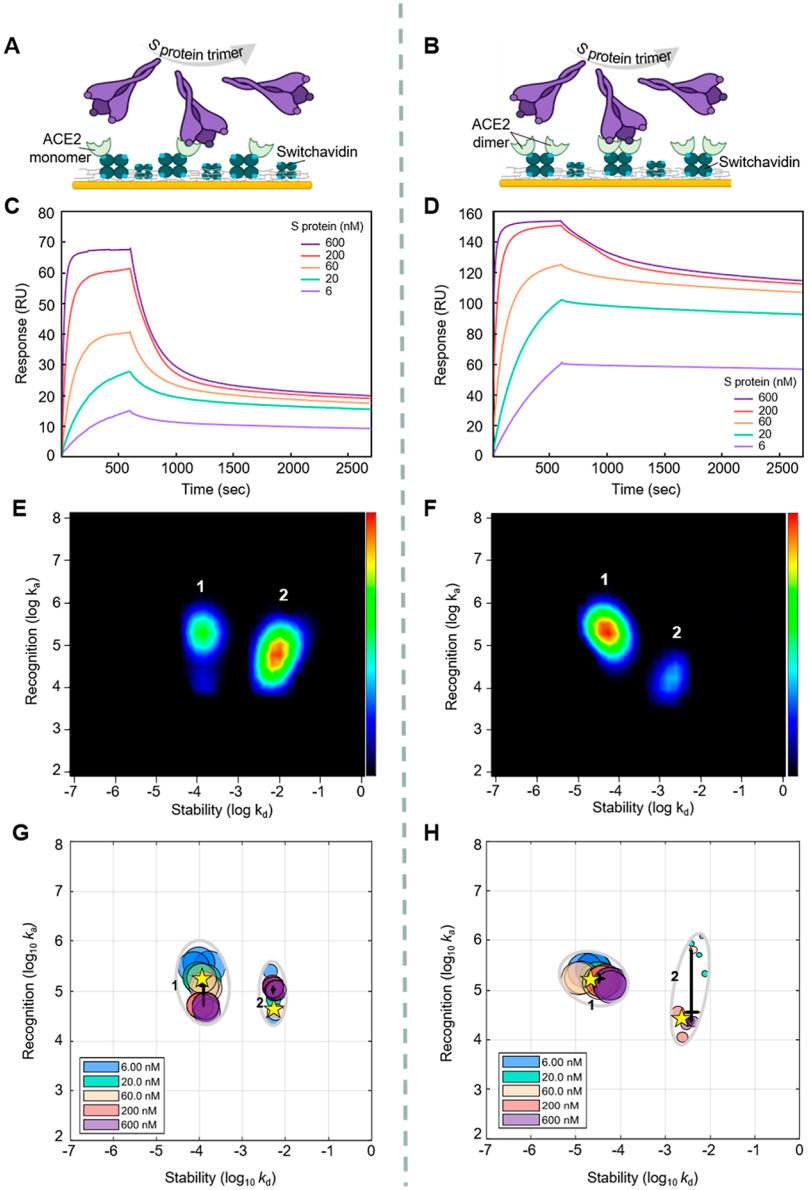

Figure 4. Multicycle kinetic sensorgrams for the SARS-CoV-2 spike ectodomain binding ACE2. (A) Schematic of the SPR assay to measure the monovalent interaction where 30 RU of monomeric ACE2 (green) was tethered to a biotin-coated sensor via a switchavidin scaffold (teal) and the trimeric S protein (purple) was injected over the surface as the analyte. (B) Schematic of the SPR assay to measure the multivalent interaction where 70 RU of dimeric ACE2 was tethered to a biotin-coated sensor. The trimeric S protein was injected over the surface as the analyte. (C,D) SPR sensorgram from a multicycle kinetic experiment where increasing concentrations of the S protein were injected over a regenerated surface for 600 s for the (C) monomeric ACE2 surface and the (D) dimeric ACE2 surface. (E,F) InteractionMap for the sensorgrams depicted in (C,D) resolved two interactions, with red corresponding to strong contributing interactions and blue corresponding to weak contributing interactions. (G,H) Cluster of individual rate constants calculated using the strategy in ref 4 to estimate the affinities observed from three replicate experiments on the (G) monomeric ACE2 surface and the (H) dimeric ACE2 surface. The circle area indicates the mean contribution of the two interactions to the total sensorgram response, and the crosses indicate the median of the clustered rate constants corresponding with 95% confidence intervals. The yellow stars indicate the rate constants estimated by global fitting. Kinetic rate constants calculated for (E–H) are summarized in Table S1. Graphics (A,B) were created with BioRender.com.

of the affinity of each interaction (Figure 4G,H). The calculated rate constants using this approach are similar to those derived using the IM, such that it calculated one 55 nM affinity interaction and a second higher-affinity interaction of around 200 pM.

CONCLUSIONS

Sensorgrams generated from multivalent interactions are a summation of distinct binding events, each with a unique combination of kinetic rate constants. A major challenge for fitting these complex sensorgrams stems from the fact that there is a large degree of heterogeneity within the system. Therefore, we set out to develop a biosensor-based method to facilitate the data deconvolution of complex SPR sensorgrams by reducing the surface heterogeneity. To do so, we isolated monomeric and multimeric ACE2 species that were scaffolded onto switchavidin using size-exclusion chromatography and mass photometry. Then, we immobilized the monomeric ACE2–switchavidin species on one surface and dimeric

https://doi.org/10.1021/acs.analchem.1c04372
Anal. Chem. 2022, 94, 1187−1194

ACE2−switchavidin on another. Using RCD analyses, we were able to resolve multiple binding events on each surface. On the dimeric ACE2 surface, the sensorgram signal is dominated by a high-affinity multivalent interaction of 283 pM with a small portion of the signal originating from the weaker monovalent interaction. Interestingly, the binding contribution from the multivalent interaction is so strong that it is also detectable on the monomeric ACE2 surface. Since the signal from the multivalent interaction is significantly weaker on the monomeric ACE2 surface, we were able to resolve a potential intermediate binding event that exists just prior to forming the high-affinity multivalent interaction. This is evident in the IM analysis where approximately 5% of the signal has a dissociation rate similar to that of the high-affinity multivalent interaction but exhibits a slower association rate. Although more work is needed, this population could represent an intermediate binding event in which the trimeric S protein is undergoing a conformational change with multiple RBDs moving into an "up" or ACE2-binding competent conformation. If our observation is a true binding intermediate, it would be consistent with a recent single-molecule fluorescence (Förster) resonance energy transfer (smFRET) study that found that the trimeric S protein shifts to an intermediate state in the presence of monomeric ACE2 where one or more RBDs shift to an upward conformation for ACE2 binding.[20] Overall, we found that reducing the surface heterogeneity in combination with a surface regeneration protocol, which repetitively provides a renewed and unaltered biosensor surface, enabled the high-resolution quantification of monovalent and multivalent interactions using two different advanced data analysis algorithms. A wide range of complex biomolecular interactions could be similarly investigated using this unprecedented biosensor approach, potentially leading to a more accurate biophysical description of biomolecular interactions.

■ ASSOCIATED CONTENT

Supporting Information

The Supporting Information is available free of charge at https://pubs.acs.org/doi/10.1021/acs.analchem.1c04372.

Summary of calculated kinetic rate constants, mass photometry calibration, SPR assays for the SARS-CoV-2 RBD binding ACE2, and additional information for the AIDA calculations (PDF)

■ AUTHOR INFORMATION

Corresponding Author

Stefan Geschwindner − *Mechanistic & Structural Biology, Discovery Sciences, R&D, AstraZeneca, SE-431 83 Mölndal, Sweden;* orcid.org/0000-0002-2154-8345; Email: stefan.geschwindner@astrazeneca.com

Authors

Aspen Rene Gutgsell − *Mechanistic & Structural Biology, Discovery Sciences, R&D, AstraZeneca, SE-431 83 Mölndal, Sweden*

Anders Gunnarsson − *Mechanistic & Structural Biology, Discovery Sciences, R&D, AstraZeneca, SE-431 83 Mölndal, Sweden*

Patrik Forssén − *Department of Engineering and Chemical Sciences, Karlstad University, SE-651 88 Karlstad, Sweden*

Euan Gordon − *Discovery Biology, Discovery Sciences, R&D, AstraZeneca, SE-431 83 Mölndal, Sweden*

Torgny Fornstedt − *Department of Engineering and Chemical Sciences, Karlstad University, SE-651 88 Karlstad, Sweden;* orcid.org/0000-0002-7123-2066

Complete contact information is available at: https://pubs.acs.org/10.1021/acs.analchem.1c04372

Author Contributions

The manuscript was written through contributions of all authors. All authors have given approval to the final version of the manuscript.

Notes

The authors declare the following competing financial interest(s): AstraZeneca authors are current or former salaried employees of AstraZeneca and have/had stock or stock options in AstraZeneca.

■ ACKNOWLEDGMENTS

A.R.G. was supported by the AstraZeneca postdoctoral program. P.F. and T.F. are grateful for the grants by the Swedish Knowledge Foundation (grant number 20170059) and by the Swedish Research Council (grant number 2015-04627). We thank David Öling for generating the SARS-CoV-2 S protein and ACE2 expression plasmids. We would also like to thank Melanie Dannemeyer, Jenny Gunnarsson, and William Lee for expression validation.

■ REFERENCES

(1) Erijman, A.; Rosenthal, E.; Shifman, J. M. *PLoS One* **2014**, *9*, No. e110085.

(2) Erlendsson, S.; Teilum, K. *Front. Mol. Biosci.* **2020**, *7*, 615565.

(3) Schasfoort, R. B. M. Introduction to Surface Plasmon Resonance. In *Handbook of Surface Plasmon Resonance*, 2nd ed.; The Royal Society of Chemistry, 2017; pp 1−26.

(4) Zhang, Y.; Forssén, P.; Fornstedt, T.; Gulliksson, M.; Dai, X. *Inverse Probl. Sci. Eng.* **2017**, *26*, 1464−1489.

(5) Forssén, P.; Samuelsson, J.; Lacki, K.; Fornstedt, T. *Anal. Chem.* **2020**, *92*, 11520−11524.

(6) Walls, A. C.; Park, Y.-J.; Tortorici, M. A.; Wall, A.; McGuire, A. T.; Veesler, D. *Cell* **2020**, *181*, 281−292.

(7) Tian, X.; Li, C.; Huang, A.; Xia, S.; Lu, S.; Shi, Z.; Lu, L.; Jiang, S.; Yang, Z.; Wu, Y.; Ying, T. *Emerging Microbes Infect.* **2020**, *9*, 382−385.

(8) Liu, L.; Chopra, P.; Li, X.; Wolfert, M. A.; Tompkins, S. M.; Boons, G. J. SARS-CoV-2 Spike Protein Binds Heparan Sulfate in a Length- and Sequence-Dependent Manner. **2020**, bioRxiv:2020.05.10.087288.

(9) Shang, J.; Ye, G.; Shi, K.; Wan, Y.; Luo, C.; Aihara, H.; Geng, Q.; Auerbach, A.; Li, F. *Nature* **2020**, *581*, 221−224.

(10) Wrapp, D.; Wang, N.; Corbett, K. S.; Goldsmith, J. A.; Hsieh, C.-L.; Abiona, O.; Graham, B. S.; McLellan, J. S. *Science* **2020**, *367*, 1260−1263.

(11) Zhu, X.; Mannar, D.; Srivastava, S. S.; Berezuk, A. M.; Demers, J.-P.; Saville, J. W.; Leopold, K.; Li, W.; Dimitrov, D. S.; Tuttle, K. S.; Zhou, S.; Chittori, S.; Subramaniam, S. Cryo-EM Structures of the N501Y SARS-CoV-2 Spike Protein in Complex with ACE2 and Two Potent Neutralizing Antibodies. *bioRxiv* **2021** DOI: 10.1101/2021.01.11.426269.

(12) Lan, J.; Ge, J.; Yu, J.; Shan, S.; Zhou, H.; Fan, S.; Zhang, Q.; Shi, X.; Wang, Q.; Zhang, L.; Wang, X. *Nature* **2020**, *581*, 215−220.

(13) Lui, I.; Zhou, X. X.; Lim, S. A.; Elledge, S. K.; Solomon, P.; Rettko, N. J.; Zha, B. S.; Kirkemo, L. L.; Gramespacher, J. A.; Liu, J.; Muecksch, F.; Lorenzi, J. C. C.; Schmidt, F.; Weisblum, Y.; Robbiani, D. F.; Nussenzweig, M. C.; Hatziioannou, T.; Bieniasz, P. D.;

Rosenburg, O. S.; Leung, K. K.; Wells, J. A. Trimeric SARS-CoV-2 Spike Interacts with Dimeric ACE2 with Limited Intra-Spike Avidity. **2020**, bioRxiv:2020.05.21.109157.
(14) Tian, F.; Tong, B.; Sun, L.; Shi, S.; Zheng, B.; Wang, Z.; Dong, X.; Zheng, P. *eLife* **2021**, *10*, No. e69091.
(15) Petersen, E.; Koopmans, M.; Go, U.; Hamer, D. H.; Petrosillo, N.; Castelli, F.; Storgaard, M.; Al Khalili, S.; Simonsen, L. *Lancet Infect. Dis.* **2020**, *20*, e238−e244.
(16) Benton, D. J.; Wrobel, A. G.; Xu, P.; Roustan, C.; Martin, S. R.; Rosenthal, P. B.; Skehel, J. J.; Gamblin, S. J. *Nature* **2020**, *588*, 327−330.
(17) Cai, Y.; Zhang, J.; Xiao, T.; Peng, H.; Sterling, S. M.; Walsh, R. M., Jr.; Rawson, S.; Rits-Volloch, S.; Chen, B. *Science* **2020**, *369*, 1586−1592.
(18) Guo, L.; Bi, W.; Wang, X.; Xu, W.; Yan, R.; Zhang, Y.; Zhao, K.; Li, Y.; Zhang, M.; Cai, X.; Jiang, S.; Xie, Y.; Zhou, Q.; Lu, L.; Dang, B. *Cell Res.* **2021**, *31*, 98−100.
(19) Zhou, T.; Tsybovsky, Y.; Gorman, J.; Rapp, M.; Cerutti, G.; Chuang, G.-Y.; Katsamba, P. S.; Sampson, J. M.; Schön, A.; Bimela, J.; Boyington, J. C.; Nazzari, A.; Olia, A. S.; Shi, W.; Sastry, M.; Stephens, T.; Stuckey, J.; Teng, I.-T.; Wang, P.; Wang, S.; Zhang, B.; Friesner, R. A.; Ho, D. D.; Mascola, J. R.; Shapiro, L.; Kwong, P. D. *Cell Host Microbe* **2020**, *28*, 867−879.
(20) Lu, M.; Uchil, P. D.; Li, W.; Zheng, D.; Terry, D. S.; Gorman, J.; Shi, W.; Zhang, B.; Zhou, T.; Ding, S.; Gasser, R.; Prévost, J.; Beaudoin-Bussières, G.; Anand, S. P.; Laumaea, A.; Grover, J. R.; Liu, L.; Ho, D. D.; Mascola, J. R.; Finzi, A.; Kwong, P. D.; Blanchard, S. C.; Mothes, W. *Cell Host Microbe* **2020**, *28*, 880−891.
(21) Forssén, P.; Multia, E.; Samuelsson, J.; Andersson, M.; Aastrup, T.; Altun, S.; Wallinder, D.; Wallbing, L.; Liangsupree, T.; Riekkola, M.-L.; Fornstedt, T. *Anal. Chem.* **2018**, *90*, 5366−5374.
(22) Altschuh, D.; Björkelund, H.; Strandgård, J.; Choulier, L.; Malmqvist, M.; Andersson, K. *Biochem. Biophys. Res. Commun.* **2012**, *428*, 74−79.
(23) Taskinen, B.; Zauner, D.; Lehtonen, S. I.; Koskinen, M.; Thomson, C.; Kähkönen, N.; Kukkurainen, S.; Määttä, J. A. E.; Ihalainen, T. O.; Kulomaa, M. S.; Gruber, H. J.; Hytönen, V. P. *Bioconjugate Chem.* **2014**, *25*, 2233−2243.
(24) Song, W.; Gui, M.; Wang, X.; Xiang, Y. *PLoS Pathog.* **2018**, *14*, No. e1007236.
(25) Young, G.; Hundt, N.; Cole, D.; Fineberg, A.; Andrecka, J.; Tyler, A.; Olerinyova, A.; Ansari, A.; Marklund, E. G.; Collier, M. P.; Chandler, S. A.; Tkachenko, O.; Allen, J.; Crispin, M.; Billington, N.; Takagi, Y.; Sellers, J. R.; Eichmann, C.; Selenko, P.; Frey, L.; Riek, R.; Galpin, M. R.; Struwe, W. B.; Benesch, J. L. P.; Kukura, P. *Science* **2018**, *360*, 423−427.
(26) Gunnarsson, A.; Stubbs, C. J.; Rawlins, P. B.; Taylor-Newman, E.; Lee, W.-c.; Geschwindner, S.; Hytönen, V.; Holdgate, G.; Jha, R.; Dahl, G. *SLAS Discovery* **2021**, *26*, 730−739.

https://doi.org/10.1021/acs.analchem.1c04372
Anal. Chem. 2022, 94, 1187−1194